SUPPORTING INFORMATION

Modulation of Fe-Fe Distance and Spin in Diiron Complexes Using Tetradentate Ligands with Different Flanking Donors†

Kyle D. Spielvogel,[a] Emily J. Campbell,[a] Sabyasachi Roy Chowdhury,[b] Florian Benner,[c] Selvan Demir,[c] Gillian P. Hatzis,[d] Hayley R. Petras,[a] Dunya Sembukuttiarachchige,[a] James J. Shepherd,[a] Christine M. Thomas,[d] Bess Vlaisavljevich,[b] and Scott R. Daly[a]*

[a]The University of Iowa, Department of Chemistry, E331 Chemistry Building, Iowa City, IA 52242, USA.

[b]The University of South Dakota, Department of Chemistry, 414 E Clark St., Vermillion SD, 57069, USA.

[c]Department of Chemistry, Michigan State University, 578 South Shaw Lane, East Lansing, Michigan 48824, USA.

[d]The Ohio State University, Department of Chemistry and Biochemistry, 100 West 18th Ave, Columbus, OH 43210, USA.

Corresponding email: scott-daly@uiowa.edu

Table of Contents

†KDS and SRD conceptualized the work and completed the synthesis and characterization of the complexes with DS. GPH and CT completed the Mossbauer studies and analysis. FB and SD collected and modelled the SQUID data. EC, HRP, JJS, SRC, and BV performed the DFT calculations at different levels of theory, and SRC and BV completed the CASPT2 calculations. KDS and SRD drafted the manuscript, and all authors contributed to editing and review.

I. Synthesis and Characterization Details

General considerations. All reactions were performed under an atmosphere of N_2 or Ar using a glovebox or standard Schlenk techniques unless stated otherwise. Pentane, diethyl ether (Et_2O), and tetrahydrofuran (thf) were dried and degassed using a Pure Process Technologies Solvent Purification System. Solvents were then stored over 3 Å sieves in the glovebox. Benzene was dried and deoxygenated by distillation from Na/benzophenone ketyl radical and subsequent freeze-pump-thaw cycles and stored over activated 3 Å molecular sieves. H_2(**L1**) and H_2(**L2**) were prepared as previously described.[1, 2] All other chemicals were purchased from commercial vendors and used as received.

Microanalytical data (CHN) were collected using an EAI CE-440 Elemental Analyzer in the UI Department of Chemistry Materials Analysis, Testing and Fabrication (MATFab) Facility. Infrared (IR) spectra were acquired on a Thermo Scientific Nicolet iS5 using an attenuated total reflectance (ATR) accessory equipped with a diamond crystal. UV-vis data were collected using an Avantes Starline AvaSpec-2048 spectrometer.

[Fe(L1)]$_2$ (1). In a glovebox, $FeCl_2$ (0.100 g, 0.789 mmol) was suspended in 15 mL of Et_2O. To the suspension was added Li[N(SiMe$_3$)$_2$] (0.264 g, 1.578 mmol) dissolved in 5 mL of Et_2O and the mixture was stirred overnight. The next day the brown solution was filtered through Celite and the volatiles were removed under vacuum to result in a tack brown solid. To the solid was added H_2(**L1**) (0.273 g, 0.790 mmol) dissolved in 15 mL of thf. The mixture was stirred overnight during which time the solution color changed to dark red. The volatiles were removed under vacuum to afford a dark red solid that was then dissolved in a minimal amount of benzene. Filtration of the dark red solution through Celite and vapor diffusion with pentane resulted in large dark red blocks. Yield: 0.241 mg, (67% based on CHN formula weight). Anal. Calcd. for $C_{44}H_{48}Fe_2N_8 \cdot (C_6H_6)_{1.5}$: C, 69.36; H, 6.26; N, 12.21. Found: C, 69.30; H, 6.25; N, 12.30. Evans

Method (C_6D_6; 293 K): 7.6 μ_B. Magnetic susceptibility balance (solid; 294 K): 7.6(1) μ_B. IR (ATR, cm^{-1}): 3052 w, 3004 w, 2957 w, 2871 w, 2830 w, 2780 w, 1586 m, 1568 s, 1472 vs, 1444 s, 1435 s, 1319 m, 1264 s, 1243 s, 1199 m, 1170 m, 1156 m, 1142 m, 1108 m, 1093 m, 1042 m, 1021 m, 921 s, 868 w, 846 m, 831 m, 757 m, 733 vs, 682 m.

[Fe(L2)]$_2$ (2). Prepared in a similar method as **1** using H_2(**L2**) (0.278 g, 0.789 mmol). Dark red crystals were grown by vapor diffusion of pentane into a concentrated benzene solution. Yield: 0.271 g, (85%). Anal. Calcd. for $C_{40}H_{36}Fe_2N_4S_4 \cdot (C_6H_6)_{1.75}$: C, 61.11; H, 4.66; N, 6.48. Found: C, 61.14; H, 4.80; N, 6.29. Evans Method (C_6D_6; 293 K): 6.3 μ_B. Magnetic susceptibility balance (solid; 294 K): 6.2(1) μ_B. IR (ATR, cm^{-1}): 3048 w, 2993 w, 2915 w, 1579 m, 1567 s, 1472 s, 1453 vs, 1426 s, 1321 s, 1282 s, 1249 s, 1233 s, 1206 s, 1176 m, 1153 m, 1123 m, 1103 m, 1068 w, 1041 m, 1032 s, 969 m, 958 m, 926 w, 906 m, 874 w, 856 w, 839 s, 827 s, 738 vs, 728 vs, 696 s, 683 s, 653 m.

II. X-ray Diffraction Studies

Single crystals retrieved from benzene/pentane (**1**, **1a**, **2**, and **2a**) were mounted on a MiTeGen micromount with ParatoneN oil. The data were collected on a Bruker Nonius Kappa CCD with an Apex II charge-coupled-device (CCD) detector (**1**, **2**, and **2a**) or a Bruker D8 Venture Duo equipped with a Bruker photon III detector (**1a**). The samples were cooled to 150 K by an Oxford Cryostreams 700 low-temperature device (Bruker Nonius Kappa CCD). The diffractometers were equipped with a graphite monochromatized Mo Kα X-ray source (λ = 0.71073). A hemisphere of data was collected using phi and omega scans. Data collection, initial indexing, and cell refinement were conducted using COLLECT[3] and DENZO/SCALEPACK[4] (Nonius Kappa CCD) or Bruker Apex II suite (Bruker Nonius Kappa CCD). The data were corrected for absorption using redundant reflections and the SADABS program.[5] Structure solution and refinement were performed in Olex2[6] using SHELXT[7] and SHELXL.[8] Hydrogen atom positions were idealized and allowed to ride on the attached carbon atom. *HKL* reflections with error/esd values ±10 were omitted from the models. The final refinement included anisotropic temperature factors on all non-hydrogen atoms. Publication figures were generated using Mercury CSD 3.10.[9] Data collection and refinement details are listed in Table S1.

Details regarding the data collection and refinement of 1a. Crystals identified as **1a** were generally of low quality and many were twinned. Data were collected on numerous crystals over the course of a week, and the data reported for **1a** are the best obtained. The finalized data contained in the CIF files did not trigger any A or B level alerts during checkCIF, but we acknowledge the relatively high residuals and R factors. Despite the lower quality of the data, we feel they are important to report given that the DFT calculations predicted the structure of **1a** and suggest that it is slightly more favorable than the structure of **1**.

Crystals of **1a**, obtained from benzene using pentane as an antisolvent, has two co-crystallized benzene molecules in the asymmetric unit cell and what appears to be disordered pentane. One of the benzene molecules was constrained to be a regular hexagon that was allowed to shrink or expand, and displacement parameters for both benzene molecules were constrained using ISOR and DELU commands to obtain satisfactory looking ellipsoids. After accounting for the two molecules of benzene, checkCIF indicated remaining solvent voids in the lattice, which corresponded to a cluster of weak Q-peaks that appear consistent with disordered pentane. A solvent mask was therefore applied. Based on the solvent mask (V = 270 Å; 56 e^-; asymmetric unit cell), we assume that there is 0.75 pentane per asymmetric unit cell. The values provided in Table S1 that depend on formula (e.g., density) do not account for the masked pentane given that we have not confirmed its identity or quantity by another method.

Table S1. Crystallographic data.

	1	**1a**	**2**	**2a**
Formula	$C_{44}H_{48}Fe_2N_8 \cdot 1.5C_6H_6$	$C_{44}H_{48}Fe_2N_8 \cdot C_6H_6$	$C_{40}H_{36}Fe_2N_4S_4$	$C_{40}H_{36}Fe_2N_4S_4 \cdot 2C_6H_6$
Identifier	dal20_19	dal22_16	dal18_80	dal18_76
FW (g mol^{-1})	917.77	878.71	812.67	968.88
crystal system	monoclinic	triclinic	monoclinic	triclinic
space group	$P2_1/c$	P-1	$P2_1/n$	P-1
a (Å)	14.1280(14)	14.495(4)	14.7925(18)	11.2216(11)
b (Å)	17.7302(18)	17.190(5)	12.1411(15)	12.4643(12)
c (Å)	18.8223(18)	20.268(7)	20.679(3)	19.1311(19)
α (deg)	90	68.265(17)	90	72.756(5)
β (deg)	101.994(5)	89.15(2)	93.443(5)	80.477(5)
γ (deg)	90	87.363(15)	90	67.034(5)
volume (Å^3)	4611.9(8)	4686(3)	3707.2(8)	968.88
Z	4	4	4	2
ρ_{calc} (g·cm^{-3})	1.322	1.245	1.456	1.370
μ (mm^{-1})	0.675	0.661	1.043	0.836
F (000)	1932	1848	1680	1008
θ range (deg)	2.212/26.35	1.899/26.595	2.350/24.82	2.502/26.487
R(int)	0.0261	0.1601	0.0809	0.0338
data/restraints/parameters	9396/0/576	19187/60/1086	7575/0/455	9528/10/541
GOF	1.040	1.024	1.030	1.039
R_1 [$I > 2\sigma(I)$][a]	0.0274	0.1036	0.0333	0.0425
wR_2 (all data)[b]	0.0731	0.3180	0.0782	0.1075
Ext. Coeff.	-	-	-	-
Largest Peak/Hole (e·Å^{-3})	0.410/-0.390	2.473/-0.772	0.310/-0.411	0.977/-0.526
Temp (K)	150(2)	150(2)	150(2)	150(2)

[a] $R_1 = \sum |F_o| - |F_c| \, | \, / \, | \sum |F_o|$ for reflections with $F_o^2 > 2\,\sigma(F_o^2)$

[b] $wR_2 = [\sum w(F_o^2 - F_c^2)^2 \, / \, \sum (F_o^2)^2]^{1/2}$ for all reflections.

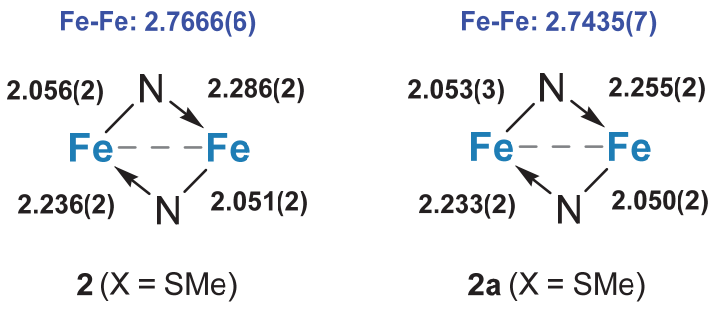

Figure S1. Comparison of XRD bond distances (Å) for **2** and the polymorph **2a**.

III. Magnetic Measurements

Magnetic susceptibility measurements were initially made on solution samples using the Evans method or on solid samples using an MSB Auto magnetic susceptibility balance purchased from Sherwood Scientific. Solid samples measured on the susceptibility balance were prepared as follows. Single crystals of **1** and **2** were ground with a mortar and pestle in an N_2-filled glovebox before packing the solids into 3.24 mm inner diameter tubes. The masses of the samples were 98.2 mg (**1**) and 95.5 mg (**2**), and the heights of the packed samples were 17.0 and 13.5 mm for **1** and **2**, respectively. The tubes were plugged with grease, removed from the glovebox, and measured on the susceptibility balance in air. A blank tube was prepared in the N_2 glovebox the same way and used to account for χ_v of the tube. Reported values and standard deviations were obtained by averaging at least eight volume magnetic susceptibility (χ_v) measurements made on the same sample at 21.0 °C. Molecular weights used for the calculations included two benzene molecules in the unit formula of **1** and **2** based on EA data and their presence in some of the crystal data. Diamagnetic corrections (χ_D) were calculated and applied using tabulated Pascal's constants for atoms and bonds.[10] The χ_D value of -3.85 x 10^{-4} emu·mol^{-1} calculated for both complexes did not include corrections for C-S and C-N bonds, but the value is relatively close to the check values of -4.78 x 10^{-4} emu·mol^{-1} (**1**) and -4.84 x 10^{-4} emu·mol^{-1} (**2**) calculated using the following approximation:

$$\chi_D \approx -\frac{MW}{2}10^{-6} emu \cdot mol^{-1}$$

where MW is the unitless molecular weight of **1** and **2**.[10]

SQUID magnetometry. Magnetic susceptibility data were obtained on a Quantum Design MPMS3 Superconducting Quantum Interference Device (SQUID) magnetometer. Samples of **1** and **2** were prepared by covering crushed crystalline solids (31.5 mg, 3.93 x 10^{-5} mol (**1**) and 23.00

mg, 2.83 x 10^{-5} mol (**2**)) with ample molten eicosane (57.3 mg (**1**) and 57.5 mg (**2**)) to prevent crystallite torquing and to provide good thermal contact between the sample and the bath. The samples were sealed airtight and transferred to the magnetometer. All data were corrected for diamagnetic contributions from the eicosane, and core diamagnetism was estimated using Pascal's constants.[10] Dc susceptibility curves were fit using the Phi software[11] written and distributed by Nicholas Chilton.

Table S2. Summary of fits of the variable-temperature dc magnetic susceptibility data for **1** to a Heisenberg exchange Hamiltonian $\widehat{H} = -2\sum\left(\hat{\vec{S}}_{Fe(1)}\bar{\bar{J}}_{Fe(1)-Fe(2)}\hat{\vec{S}}_{Fe(2)}\right) + \mu_B\sum_{i=1}^{N}\left(\sigma_i\vec{L}_i\bar{\bar{I}} + \hat{\vec{S}}_i\bar{\bar{g}}_l\right)\vec{B}$ as implemented in Phi.[11] $\bar{\bar{J}}_{Fe(1)-Fe(2)}$ accounts for the exchange tensor ascribed to the intramolecular Fe^{II}–Fe^{II} coupling, $\hat{\vec{S}}_i$ are the spin operators for each Fe^{II} ion, σ_i is an orbital reduction factor, $\vec{L}_i$ is the orbital angular momentum operator, $\bar{\bar{I}}$ is the identity matrix, $\bar{\bar{g}}_l$ is the g tensor. Settings for Fe(II) ions were chosen as implemented for O_h symmetry with weak crystal field ($S = 2$, $L = 1$).

	1.0 T	
Temperature Range	**2-300 K**	**30-300 K**
g	1.847(2)	1.825(2)
***J* (cm^{-1})**	−0.300(3)	−0.22(3)

Table S3. Summary of fits of the variable-temperature dc magnetic susceptibility data for **2** to a Heisenberg exchange Hamiltonian $\widehat{H} = -2\sum\left(\hat{\vec{S}}_{Fe(1)}\bar{\bar{J}}_{Fe(1)-Fe(2)}\hat{\vec{S}}_{Fe(2)}\right) + \mu_B\sum_{i=1}^{N}\left(\sigma_i\vec{L}_i\bar{\bar{I}} + \hat{\vec{S}}_i\bar{\bar{g}}_l\right)\vec{B}$ where the first term describes the exchange interaction and the second term the Zeeman effect as implemented in Phi.[11]

	1.0 T	
Temperature Range	**2-300 K**	**30-300 K**
g	2.25(4)	2.31(5)
***J* (cm^{-1})**	−35(1)	−37(1)

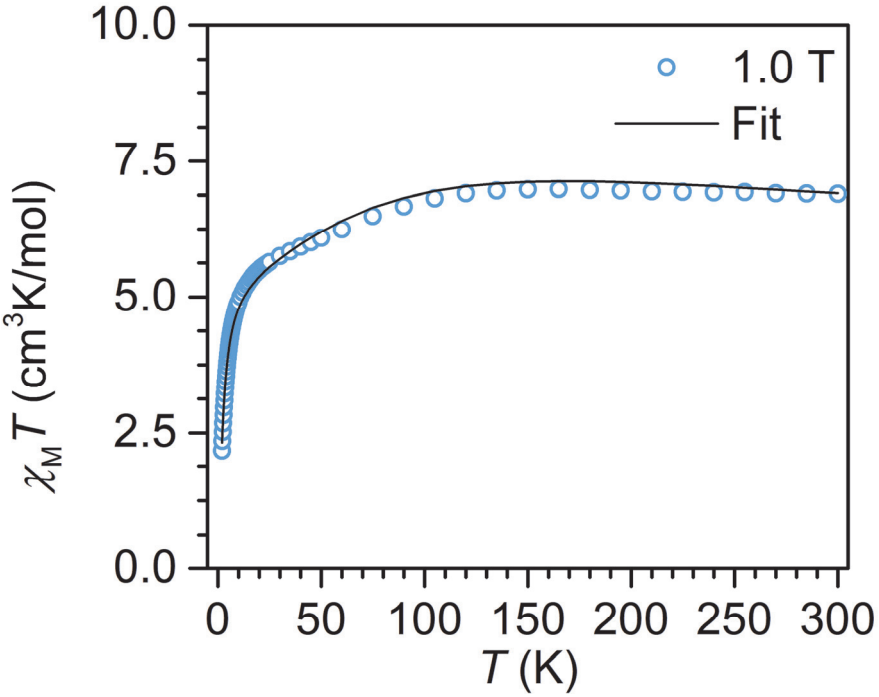

Figure S2. Variable-temperature dc magnetic susceptibility data for a restrained polycrystalline sample of **1** collected under a 1.0 T applied dc field. The black line represents a fit to the data from 2 to 300 K.

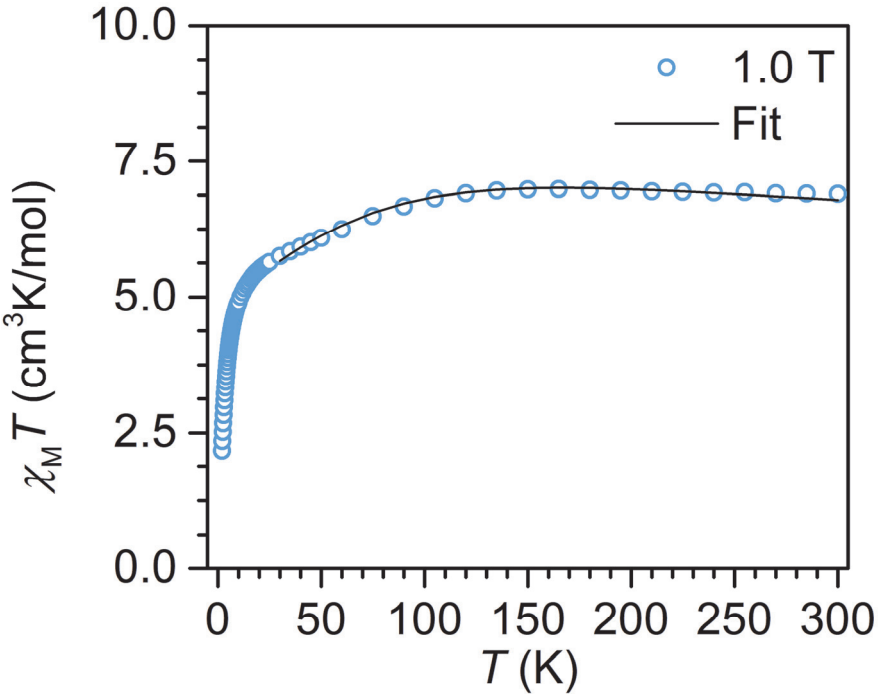

Figure S3. Variable-temperature dc magnetic susceptibility data for a restrained polycrystalline sample of **1** collected under a 1.0 T applied dc field. The black line represents a fit to the data from 30 to 300 K.

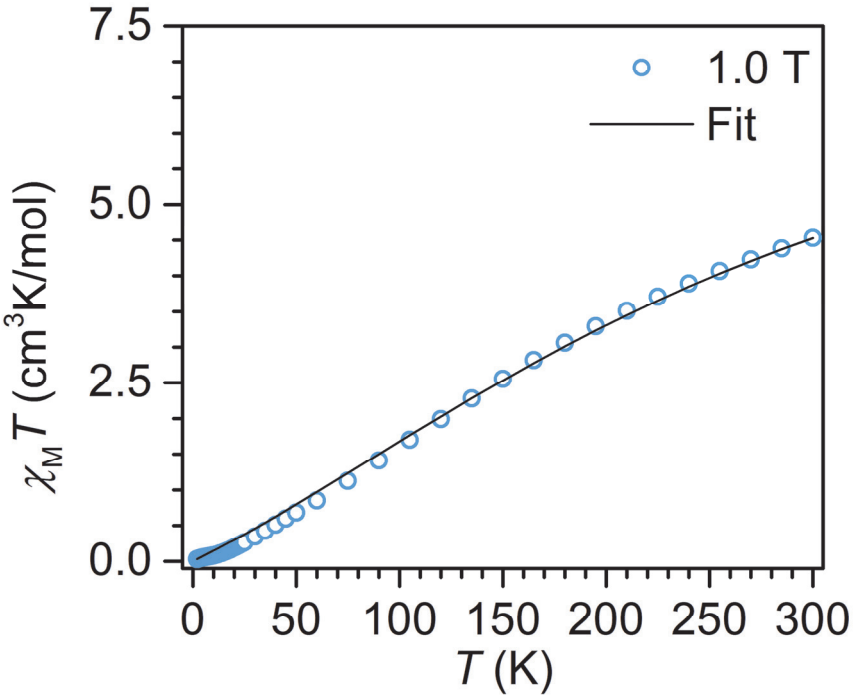

Figure S4. Variable-temperature dc magnetic susceptibility data for a restrained polycrystalline sample of **2** collected under a 1.0 T applied dc field. The black line represents a fit to the data from 2 to 300 K.

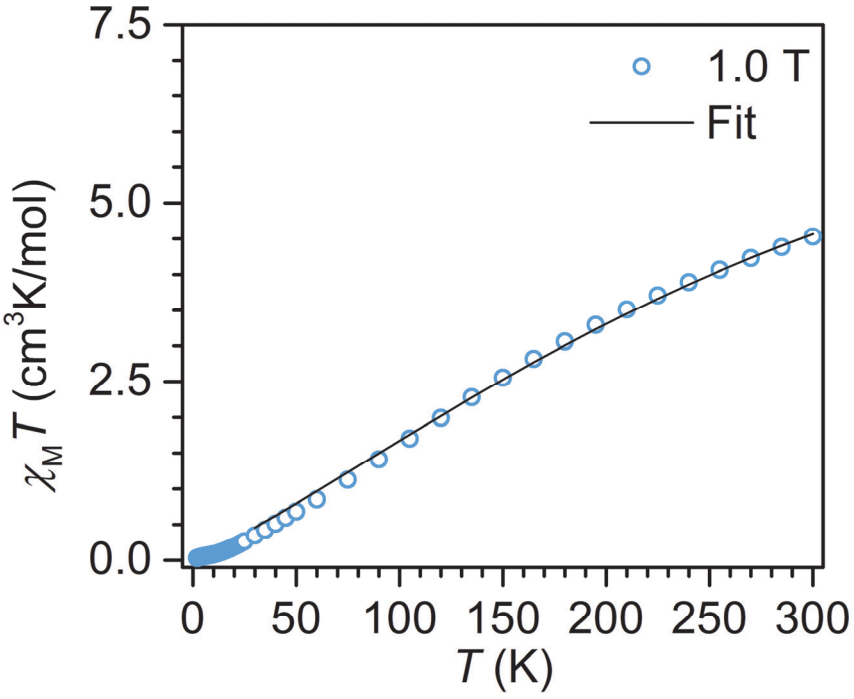

Figure S5. Variable-temperature dc magnetic susceptibility data for a restrained polycrystalline sample of **2** collected under a 1.0 T applied dc field. The black line represents a fit to the data from 30 to 300 K.

IV. ^{57}Fe Mössbauer Spectroscopy

Samples for ^{57}Fe Mössbauer spectroscopy were prepared by suspending approximately 30 mg of sample in Paratone®-N cryoprotectant oil in a cup and loading into the sample holder under liquid N_2. Spectra were obtained under zero applied field at the specified temperature (4 K or 20 K) over a 24-hour period using a See Co. (Minneapolis, MN) constant-acceleration spectrometer equipped with a Janis SHI-4 cryostat. Isomer shifts (δ) are reported relative to a 25-μm thick sample of α-Fe foil at 295 K. Data folding and fitting routines were performed using the WMOSS-4F software package.[12]

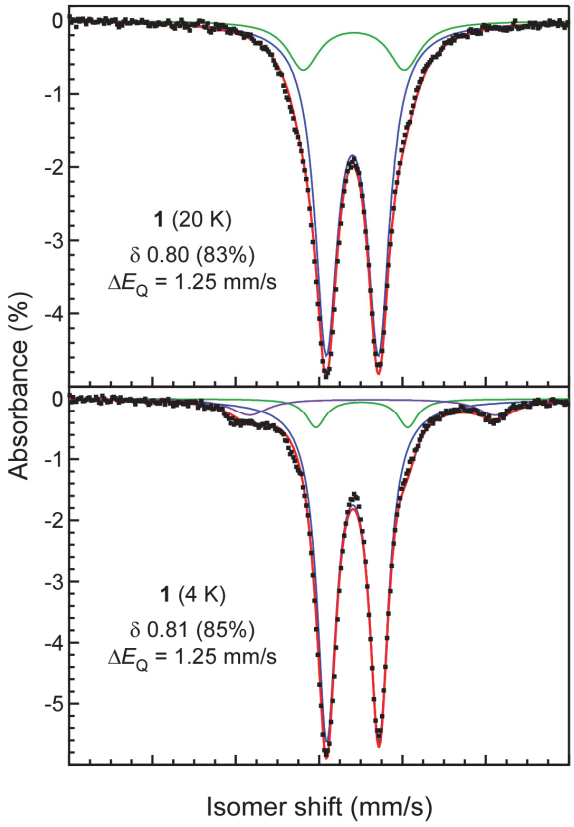

Figure S6. Comparison of ^{57}Fe Mössbauer spectra collected for **1** at 4 K and 20 K. Data points are shown as blacks squares and fits are shown as red traces. Fit at 20 K: major component (blue trace; 83%), δ 0.80, ΔE_Q = 1.25 mm/s; minor component (green trace, 17%), δ 0.84, ΔE_Q = 2.43 mm/s. Fit at 4 K: major component (blue trace; 85%), δ 0.81, ΔE_Q = 1.25 mm/s; minor component 1 (green trace, 7%), δ 1.02, ΔE_Q = 2.20 mm/s; minor component 2 (purple trace, 8%), δ 1.28, ΔE_Q = 5.90 mm/s.

V. UV-vis Spectra

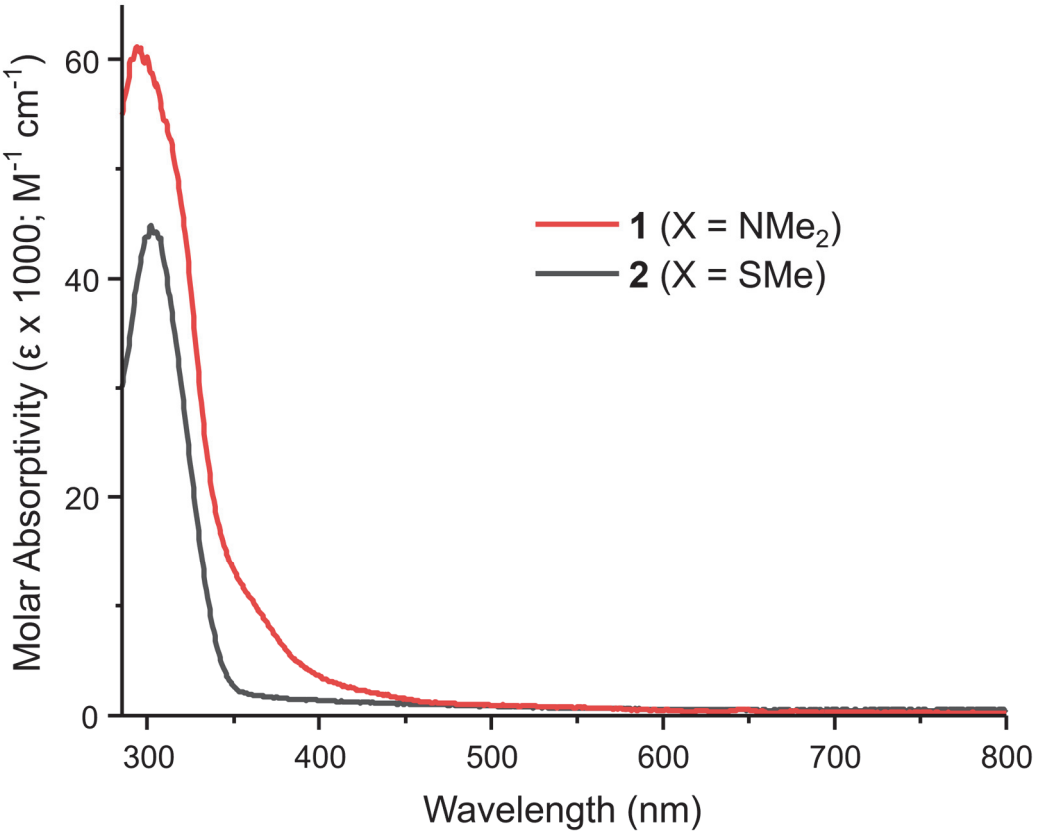

Figure S7. UV-vis spectra for **1** and **2** in benzene.

VI. Computational Details

The molecular geometry optimizations of all the complexes were carried out using density functional theory. The B3LYP[13-15] functional in conjunction with the def2-TZVP[16] basis set was used on all the atoms. For each geometry optimization, the convergence threshold to the cartesian gradient was set to 1 x 10^{-4}. Grimme's D3 dispersion correction with the original damping function was used throughout all the calculations.[17] All the fully optimized geometries were confirmed as minima by harmonic vibrational analysis. The partial optimization of the complex **1′** was performed by freezing the coordinates of the metal ions at the experimental positions. To compare the sensitivity of the DFT functionals on the relative energy differences between **1′** and **1a**, single point energies were evaluated with M06,[18] PBE0-D3,[19] and TPSSh-D3[20, 21] functionals on the B3LYP-D3 computed **1′** and **1a** geometries. The resolution of identity (RI)[22] approximation was also employed for the integral evaluations. All the DFT optimizations were performed with the Turbomole program package.[23] The information obtained from the Turbomole calculations was subjected to Multiwfn[24] program to evaluate the Mayer bond-order[25] between the metal ions in all three complexes.

For the wave function-based analysis, the DFT optimized geometry was subjected to the complete active space self-consistent field (CASSCF)[26, 27] calculations. The active space includes eight electrons distributed over sixteen *d*-orbitals (8e,16o) (Figure S8). The CASSCF calculations were performed over the lowest energy singlet, triplet, quintet, septet, and nonet states. The scalar relativistic effects were included using the second-order Douglas-Kroll-Hess Hamiltonian[28] and relativistic all-electron ANO-RCC basis sets.[29, 30] The first coordination sphere was treated with the ANO-RCC-VTZP basis set, and the remaining elements were described by ANO-RCC-MB basis sets. Specifically, we use [6s,5p,3d,2f,1g] contraction for iron, [4s,3p,2d,1f] for nitrogen, [5s,4p,2d,1f] for sulfur, [2s,1p] for carbons and [1s] for hydrogens. Cholesky decomposition[31] in

conjunction with local-exchange screening was used to reduce the computational cost. The CASSCF wave functions were subjected to complete active space second-order perturbation theory (CASPT2)[32, 33] calculations to evaluate the effect of dynamic electron correlation in the spin state energetics of the molecule. In the CASPT2 calculations, the standard definition of the zero-order Hamiltonian (IPEA = 0.25 a.u) is used.[34] To exclude the possible intruder states an imaginary shift of 0.2 a.u. was applied. All the CASSCF and CASPT2 calculations were carried out using the OpenMolcas software suite.[35]

Table S4. B3LYP-D3/def2-TZVP computed Fe-Fe and Fe-N distances of the complexes under investigation. The respective experimental distances are in brackets.

Complex	Fe-Fe (Å)	Fe-N (Å)	Fe→N (Å)
1′	2.507 [2.5072(5)]	2.069 [2.082(1)] 2.067 [2.097(1)]	2.355 [2.290(1)] 2.364 [2.305(1)]
1a	2.687 [2.627(2)]	2.015 [2.011(6)] 2.014 [2.029(6)]	2.631 [2.489(6)] 2.633 [2.551(7)]
2	2.807 [2.7666(6)]	2.049 [2.056(2)] 2.049 [2.051(2)]	2.346 [2.236(2)] 2.349 [2.286(2)]

Table S5. The total energies computed by the DFT and CASPT2 methods at their respective lowest energy state. Relative energy differences between the **1′** and **1a** reported.

Method	**2S+1**	$\mathbf{E^{1'}}$ a.u.	$\mathbf{E^{1a}}$ a.u.	ΔE kcal/mol
B3LYP-D3	9	-4670.60252440	-4670.60784103	3.3
CASPT2	1	-4677.33874444	-4677.34764062	5.6

Table S6. The relative energy differences between **1′** and **1a**, computed by M06, TPSSh-D3, and PBE0-D3 functionals on the B3LYP-D3 optimized geometries.

Functional	**2S+1**	$\mathbf{E^{1'}}$ a.u.	$\mathbf{E^{1a}}$ a.u.	ΔE kcal/mol
M06	9	-4670.25450586	-4670.25859140	2.6
PBE0-D3	9	-4669.06093490	-4669.06651858	3.5
TPSSh-D3	9	-4672.26621350	-4672.27144596	3.3

Table S7. B3LYP-D3/def2-TZVP energies for different spin states computed on the S=4 geometries of the complexes **1′**, **1a**, and **2**.

2S+1	**1′**		**1a**		**2**	
	E a.u.	ΔE kcal/mol	E a.u.	ΔE kcal/mol	E a.u.	ΔE kcal/mol
9	**-4670.60252440**	0.0	**-4670.60784103**	0.0	**-5884.70930239**	0.0
7	-4670.57516470	17.2	-4670.57996825	17.5	-5884.68040344	18.1
5	-4670.56360887	24.4	-4670.54810611	37.5	-5884.65221595	35.8
3	-4670.52827445	46.6	-4670.53441582	46.1	-5884.64093331	42.9
1	-4670.48796502	71.9	-4670.48071337	79.8	-5884.59936830	69.0

Table S8. $<S^2>$ values corresponding to the B3LYP-D3/def2-TZVP calculations in Table S5.

2S+1	**Exact $<S^2>$**	**1′**	**1a**	**2**
9	20	20.0	20.0	20.0
7	12	12.3	12.4	12.3
5	6	7.2	6.7	6.5
3	2	3.6	3.8	3.5
1	0	0.0	0.0	0.0

Table S9. CASPT2 energies for different spin states computed on the B3LYP-D3/def2-TZVP optimized geometries of the complexes **1′**, **1a**, and **2**.

	1′		**1a**		**2**	
2S+1	E a.u.	ΔE kcal/mol	E a.u.	ΔE kcal/mol	E a.u.	ΔE kcal/mol
9	-4677.33712884	1.0	-4677.34714632	0.3	-5895.26934587	0.3
7	-4677.33680985	1.2	-4677.34648882	0.7	-5895.26863891	0.7
5	-4677.33736701	0.9	-4677.34668182	0.6	-5895.26880357	0.6
3	-4677.33806097	0.4	-4677.34708231	0.4	-5895.26921015	0.3
1	**-4677.33874444**	0.0	**-4677.34764062**	0.0	**-5895.26975265**	0.0

Table S10. The Mayer bond-orders between the metal ions in complexes **1′**, **1a**, and **2**.

Complex	**Bond-Order**
1′	0.11
1a	0.13
2	0.05

Table S11. Percent contributions from some of the Hartree-Fock determinants to the CASSCF wavefunction for complex **1′** at its singlet spin state. 2 = Doubly Occupied, 0 = Unoccupied, u = singly occupied up-spin, d = singly occupied down-spin.

Hartree-Fock Determinants (M.O. 1—16)	% Contribution
2222000000000000	1.8
2202200000000000	2.6
u2d2ud0000000000	2.1
0222020000000000	1.7
0202220000000000	2.3

Table S12. Percent contributions from some of the Hartree-Fock determinants to the CASSCF wavefunction for complex **1a** at its singlet spin state. 2 = Doubly Occupied, 0 = Unoccupied, u = singly occupied up-spin, d = singly occupied down-spin.

Hartree-Fock Determinants (M.O. 1—16)	% Contribution
2222000000000000	1.8
2202200000000000	2.4
u2d2ud0000000000	1.9
0222020000000000	1.7
0202220000000000	2.2

Table S13. Percent contributions from some of the Hartree-Fock determinants to the CASSCF wavefunction for complex **2** at its singlet spin state. 2 = Doubly Occupied, 0 = Unoccupied, u = singly occupied up-spin, d = singly occupied down-spin.

Hartree-Fock Determinants (M.O. 1—16)	% Contribution
2022002000000000	1.7
0222002000000000	2.0
uud2d02000000000	2.6
2022020000000000	1.9
0202202000000000	2.3

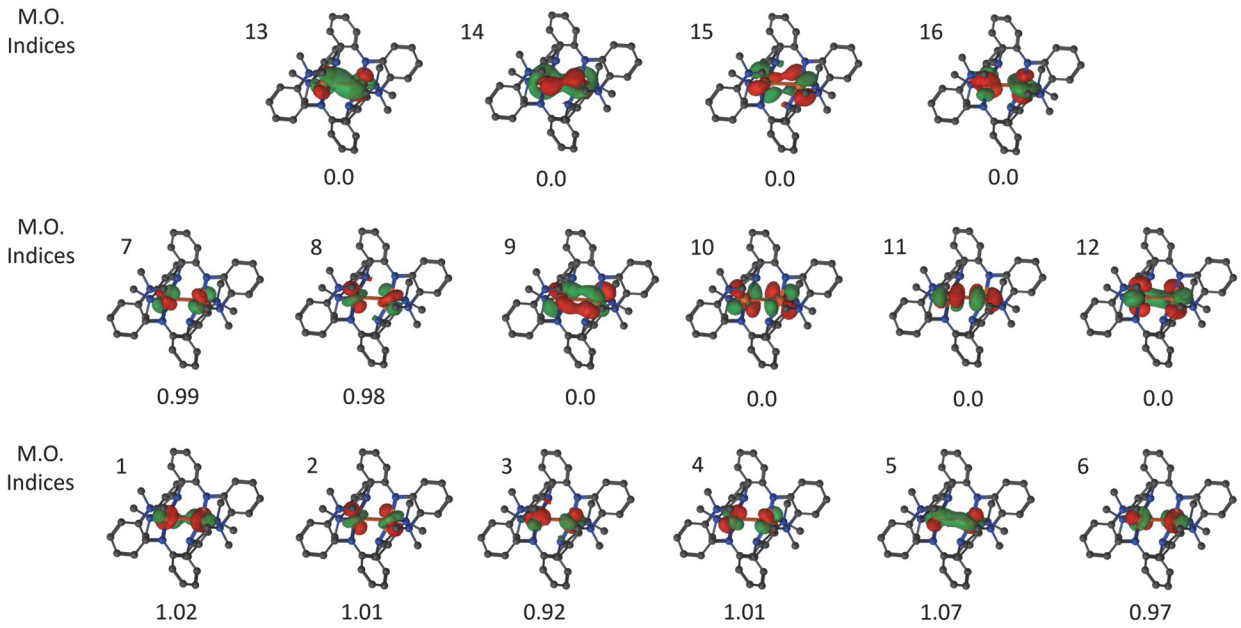

Figure S8. CASSCF active natural orbitals of **1a** from the (8*e*,16*o*) active space computed for the lowest energy singlet state, as determined by the CASPT2 calculations. An isosurface value of 0.04 a.u. was used. Occupation numbers of the orbitals are included. Active orbitals are not reported for the other complexes and spin states since a qualitatively similar picture emerges in all cases.

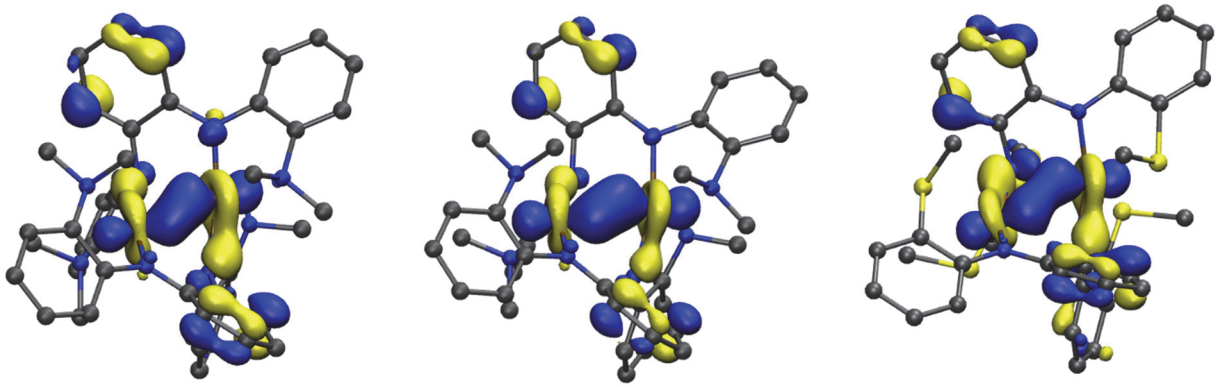

Figure S9. The B3LYP-D3/def2-TZVP computed HOMO-13 orbitals of complexes (a) **1′**, (b) **1a**, and (c) **2**.

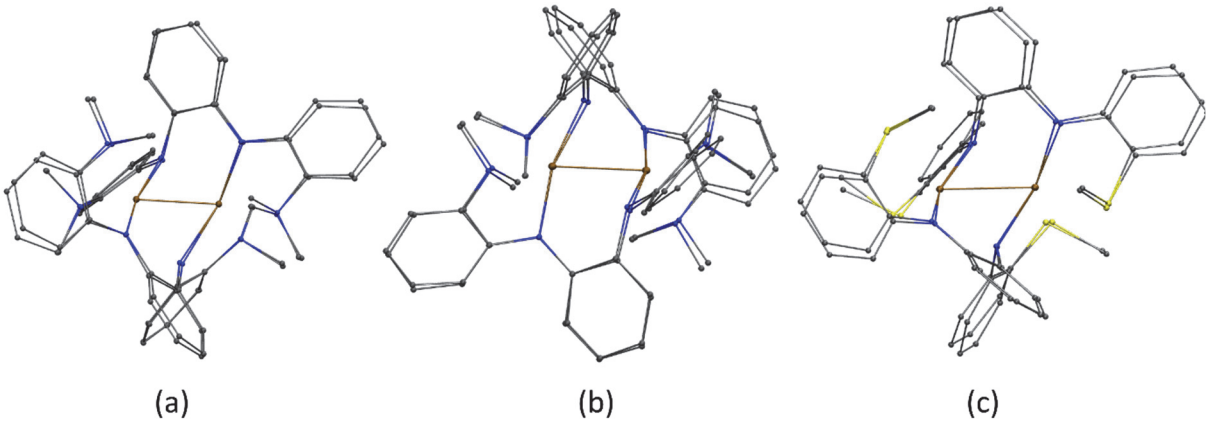

Figure S10. An overlay diagram of the computed and experimental structures of the complexes (a) **1** and **1′**, (b) **1a**, and (c) **2**. The Fe, C, N, and S atoms are in brown, grey, blue, and yellow, respectively. The hydrogens are removed for clarity.

VII. Supporting Information References

(1) Spielvogel, K. D.; Coughlin, E. J.; Petras, H.; Luna, J. A.; Benson, A.; Donahue, C. M.; Kibasa, A.; Lee, K.; Salacinski, R.; Bart, S. C.; Shaw, S. K.; Shepherd, J. J.; Daly, S. R. The Influence of Redox-Innocent Donor Groups in Tetradentate Ligands Derived from *o*-Phenylenediamine: Electronic Structure Investigations with Nickel. *Inorg. Chem.* **2019**, *58*, 12756-12774.

(2) Durgaprasad, G.; Luna, J. A.; Spielvogel, K. D.; Haas, C.; Shaw, S. K.; Daly, S. R. Ru(II) Complexes with a Chemical and Redox-Active S_2N_2 Ligand: Structures, Electrochemistry, and Metal–Ligand Cooperativity. *Organometallics* **2017**, *36*, 4020-4031.

(3) Hooft, R. W. W. COLLECT. Nonius BV, Delft, The Netherlands. *Acta Crystallographica Section E Structure Reports Online ISSN* **1998**, 1600-5368.

(4) Otwinowski, Z.; Minor, W. i. Methods in Enzymology, Vol. 276, Macromolecular Crystallography, Part A, edited by CW Carter Jr & RM Sweet. New York: Academic Press: 1997.

(5) Bruker. SADABS v.2.03. *Bruker AXS Inc., Madison, WI, USA* **2001**.

(6) Dolomanov, O. V.; Bourhis, L. J.; Gildea, R. J.; Howard, J. A. K.; Puschmann, H. OLEX2: a complete structure solution, refinement and analysis program. *Journal of Applied Crystallography* **2009**, *42*, 339-341.

(7) Sheldrick, G. M. SHELXT–Integrated space-group and crystal-structure determination. *Acta Crystallographica Section A: Foundations and Advances* **2015**, *71*, 3-8.

(8) Sheldrick, G. M. Crystal structure refinement with SHELXL. *Acta Crystallographica Section C: Structural Chemistry* **2015**, *71*, 3-8.

(9) Macrae, C. F.; Edgington, P. R.; McCabe, P.; Pidcock, E.; Shields, G. P.; Taylor, R.; Towler, M.; van de Streek, J. Mercury: visualization and analysis of crystal structures. *Journal of Applied Crystallography* **2006**, *39*, 453-457.

(10) Bain, G. A.; Berry, J. F. Diamagnetic Corrections and Pascal's Constants. *J. Chem. Ed.* **2008**, *85*, 532.

(11) Chilton, N. F.; Anderson, R. P.; Turner, L. D.; Soncini, A.; Murray, K. S. PHI: A powerful new program for the analysis of anisotropic monomeric and exchange-coupled polynuclear d- and f-block complexes. *J. Comput. Chem.* **2013**, *34*, 1164-1175.

(12) Prisecaru, I. *WMOSS4 Mössbauer Spectral Analysis Software*, www.wmoss.org, 2016.

(13) Becke, A. D. Density-functional thermochemistry. IV. A new dynamical correlation functional and implications for exact-exchange mixing. *J. Chem. Phys.* **1996**, *104*, 1040-1046.

(14) Becke, A. D. Density-functional thermochemistry. V. Systematic optimization of exchange-correlation functionals. *J. Chem. Phys.* **1997**, *107*, 8554-8560.

(15) Lee, C.; Yang, W.; Parr, R. G. Development of the Colle-Salvetti correlation-energy formula into a functional of the electron density. *Phys. Rev. B Condens. Matter* **1988**, *37*, 785-789.

(16) Weigend, F.; Ahlrichs, R. Balanced basis sets of split valence, triple zeta valence and quadruple zeta valence quality for H to Rn: Design and assessment of accuracy. *Phys. Chem. Chem. Phys.* **2005**, *7*, 3297-3305.

(17) Caldeweyher, E.; Bannwarth, C.; Grimme, S. Extension of the D3 dispersion coefficient model. *J. Chem. Phys.* **2017**, *147*, 034112.

(18) Zhao, Y.; Truhlar, D. G. The M06 suite of density functionals for main group thermochemistry, thermochemical kinetics, noncovalent interactions, excited states, and transition elements: two new functionals and systematic testing of four M06-class functionals and 12 other functionals. *Theor. Chem. Acc.* **2008**, *120*, 215-241.

(19) Adamo, C.; Barone, V. Toward reliable density functional methods without adjustable parameters: The PBE0 model. *J. Chem. Phys.* **1999**, *110*, 6158-6170.

(20) Tao, J.; Perdew, J. P.; Staroverov, V. N.; Scuseria, G. E. Climbing the Density Functional Ladder: Nonempirical Meta--Generalized Gradient Approximation Designed for Molecules and Solids. *Phys. Rev. Lett.* **2003**, *91*, 146401.

(21) Staroverov, V. N.; Scuseria, G. E.; Tao, J.; Perdew, J. P. Erratum: "Comparative assessment of a new nonempirical density functional: Molecules and hydrogen-bonded complexes" [J. Chem. Phys. 119, 12129 (2003)]. *J. Chem. Phys.* **2004**, *121*, 11507-11507.

(22) Eichkorn, K.; Treutler, O.; Oehm, H.; Haeser, M.; Ahlrichs, R. Auxiliary basis sets to approximate Coulomb potentials. *Chem. Phys. Lett.* **1995**, *240*, 283-290.

(23) Ahlrichs, R. *et al. TURBOMOLE*, version 7.3; Universität Karlsruhe, 2018

(24) Lu, T.; Chen, F. Multiwfn: A multifunctional wavefunction analyzer. *J. Comput. Chem.* **2012**, *33*, 580-592.

(25) Mayer, I. Charge, bond order and valence in the AB initio SCF theory. *Chem. Phys. Lett.* **1983**, *97*, 270-274.

(26) Roos, B. O. The complete active space SCF method in a fock-matrix-based super-CI formulation. *Int. J. Quantum Chem.* **1980**, *18*, 175-189.

(27) Roos, B. O.; Taylor, P. R.; Sigbahn, P. E. M. A complete active space SCF method (CASSCF) using a density matrix formulated super-CI approach. *Chem. Phys.* **1980**, *48*, 157-173.

(28) Hess, B. A. Relativistic electronic-structure calculations employing a two-component no-pair formalism with external-field projection operators. *Phys. Rev. A* **1986**, *33*, 3742-3748.

(29) Roos, B. O.; Lindh, R.; Malmqvist, P.-Å.; Veryazov, V.; Widmark, P.-O. Main Group Atoms and Dimers Studied with a New Relativistic ANO Basis Set. *J. Phys. Chem. A* **2004**, *108*, 2851-2858.

(30) Roos, B. O.; Veryazov, V.; Widmark, P.-O. Relativistic atomic natural orbital type basis sets for the alkaline and alkaline-earth atoms applied to the ground-state potentials for the corresponding dimers. *Theor. Chem. Acc.* **2004**, *111*, 345-351.

(31) Aquilante, F.; Malmqvist, P.-Å.; Pedersen, T. B.; Ghosh, A.; Roos, B. O. Cholesky Decomposition-Based Multiconfiguration Second-Order Perturbation Theory (CD-CASPT2): Application to the Spin-State Energetics of Co^{III}(diiminato)(NPh). *J. Chem. Theory Comput.* **2008**, *4*, 694-702.

(32) Andersson, K.; Malmqvist, P. Å.; Roos, B. O. Second-order perturbation theory with a complete active space self-consistent field reference function. *J. Chem. Phys.* **1992**, *96*, 1218-1226.

(33) Andersson, K.; Malmqvist, P. A.; Roos, B. O.; Sadlej, A. J.; Wolinski, K. Second-order perturbation theory with a CASSCF reference function. *J. Phys. Chem.* **1990**, *94*, 5483-5488.

(34) Ghigo, G.; Roos, B. O.; Malmqvist, P.-Å. A modified definition of the zeroth-order Hamiltonian in multiconfigurational perturbation theory (CASPT2). *Chem. Phys. Lett.* **2004**, *396*, 142-149.

(35) Li Manni, G.; Fdez. Galván, I.; Alavi, A.; Aleotti, F.; Aquilante, F.; Autschbach, J.; Avagliano, D.; Baiardi, A.; Bao, J. J.; Battaglia, S.; Birnoschi, L.; Blanco-González, A.; Bokarev, S. I.; Broer, R.; Cacciari, R.; Calio, P. B.; Carlson, R. K.; Carvalho Couto, R.; Cerdán, L.; Chibotaru, L. F.; Chilton, N. F.; Church, J. R.; Conti, I.; Coriani, S.; Cuéllar-Zuquin, J.; Daoud, R. E.; Dattani, N.; Decleva, P.; de Graaf, C.; Delcey, M. G.; De Vico, L.; Dobrautz, W.; Dong, S. S.; Feng, R.; Ferré, N.; Filatov, M.; Gagliardi, L.; Garavelli, M.; González, L.; Guan, Y.; Guo, M.; Hennefarth, M. R.; Hermes, M. R.; Hoyer, C. E.; Huix-Rotllant, M.; Jaiswal, V. K.; Kaiser, A.; Kaliakin, D. S.; Khamesian, M.; King, D. S.; Kochetov, V.; Krośnicki, M.; Kumaar, A. A.; Larsson, E. D.; Lehtola, S.; Lepetit, M.-B.; Lischka, H.; López Ríos, P.; Lundberg, M.; Ma, D.; Mai, S.; Marquetand, P.; Merritt, I. C. D.; Montorsi, F.; Mörchen, M.; Nenov, A.; Nguyen, V. H. A.; Nishimoto, Y.; Oakley, M. S.; Olivucci, M.; Oppel, M.; Padula, D.; Pandharkar, R.; Phung, Q. M.; Plasser, F.; Raggi, G.; Rebolini, E.; Reiher, M.; Rivalta, I.; Roca-Sanjuán, D.; Romig, T.; Safari, A. A.; Sánchez-Mansilla, A.; Sand, A. M.; Schapiro, I.; Scott, T. R.; Segarra-Martí, J.; Segatta, F.; Sergentu, D.-C.; Sharma, P.; Shepard, R.; Shu, Y.; Staab, J. K.; Straatsma, T. P.; Sørensen, L. K.; Tenorio, B. N. C.; Truhlar, D. G.; Ungur, L.; Vacher, M.; Veryazov, V.; Voß, T. A.; Weser, O.; Wu, D.; Yang, X.; Yarkony, D.; Zhou, C.; Zobel, J. P.; Lindh, R. The OpenMolcas Web: A Community-Driven Approach to Advancing Computational Chemistry. *J. Chem. Theory Comput.* **2023**.